

# Multi-centred Strong Augmentation via Contrastive Learning for Unsupervised Lesion Detection and Segmentation

Yu Tian, Fengbei Liu, Guansong Pang, Yuanhong Chen, Yuyuan Liu, Johan W. Verjans, Rajvinder Singh and Gustavo Carneiro

**Abstract**—The scarcity of high quality medical image annotations hinders the implementation of accurate clinical applications for detecting and segmenting abnormal lesions. To mitigate this issue, the scientific community is working on the development of unsupervised anomaly detection (UAD) systems that learn from a training set containing only normal (i.e., healthy) images, where abnormal samples (i.e., unhealthy) are detected and segmented based on how much they deviate from the learned distribution of normal samples. One significant challenge faced by UAD methods is how to learn effective low-dimensional image representations that are sensitive enough to detect and segment abnormal lesions of varying size, appearance and shape. To address this challenge, we propose a novel self-supervised UAD pre-training algorithm, named **Multi-centred Strong Augmentation via Contrastive Learning (MSACL)**. MSACL learns representations by separating several types of strong and weak augmentations of normal image samples, where the weak augmentations represent normal images and strong augmentations denote synthetic abnormal images. To produce such strong augmentations, we introduce MedMix, a novel data augmentation strategy that creates new training images with realistic looking lesions (i.e., anomalies) in normal images. The pre-trained representations from MSACL are generic and can be used to improve the efficacy of different types of off-the-shelf state-of-the-art (SOTA) UAD models. Comprehensive experimental results show that the use of MSACL largely improves these SOTA UAD models on four medical imaging datasets from diverse organs, namely colonoscopy, fundus screening and covid-19 chest-ray datasets. Code will be made publicly available upon paper acceptance.

**Index Terms**—Unsupervised Anomaly Detection, Anomaly Segmentation, One-class Classification, Covid-19, Colonoscopy, Fundus Image

## I. INTRODUCTION AND BACKGROUND

**D**ETECTING and segmenting malignant lesions is a crucial task in the analysis of medical images. Modern computer aided systems, based on deep learning techniques, play a critical role in assisting and accelerating such process [1]–[9].

This work was supported by Australian Research Council through grants DP180103232, and FT190100525. Y. Tian and F. Liu contributed equally to this work. Y. Tian is the corresponding author with email address: yu.tian01@adelaide.edu.au

Y. Tian, F. Liu, G. Pang, Y. Chen, Y. Liu, J. W. Verjans and G. Carneiro are with the Australian Institute for Machine Learning, University of Adelaide, Australia. R. Singh is with the Faculty of Health and Medical Sciences, University of Adelaide, Australia. Y. Tian and J. W. Verjans are also with the South Australian Health and Medical Research Institute, Australia.

Such systems are useful in health screening programs that require clinicians to analyse large quantities of images [10], [11], where the majority consist of normal (or healthy) cases, and a small minority represent abnormal (or unhealthy) cases that can be regarded as anomalies. Constraining the development of these systems on the collection and annotation of such class-imbalanced training sets is challenging and time-consuming, so it is important to consider a more efficient alternative that uses a training set containing exclusively normal samples. One advantage of this alternative approach is that the acquisition of such training set is straightforward given the large proportion of healthy subjects in health screening programs. The lesion detection and segmentation method modelled with a training set containing only normal cases is known as a unsupervised anomaly detection (UAD) method [12]–[14].

UAD methods aim to train an anomaly classifier with normal class samples only. Test image anomalies (or abnormal cases) are detected based on the extent that they deviate from the distribution of normal samples. Popular anomaly detection approaches [2], [13]–[21] can be generally divided into two categories: predictive-based methods (e.g., deep support vector data description (DSVDD) [22], one-class support vector machine (OC-SVM) [23], and deviation network [21]), and generative-based methods (e.g., auto-encoder (AE) [13], [14], [17], [19] and generative adversarial network (GAN) [3], [15], [24]). Predictive-based UAD approaches train a one-class classifier to describe the distribution of normal data, and discriminate abnormal data using their distance/deviation to the normal data distribution; whereas generative-based UAD approaches train deep generative models to learn latent representations of normal images, and detect anomalies based on the reconstruction error constrained by learned latent representation distribution [25]. One fundamental problem in both types of UAD methods is to learn expressive feature representations of images. To detect lesions in medical images, this problem is particularly critical because anomalous lesions may show only subtle deviations from normal tissue (e.g., tiny and flat colon polyps) [2]. If not well trained, these UAD models can overfit the normal training data and learn ineffective image representations, failing to detect and segment subtle abnormal lesions. Previous papers tackle this problem using ImageNet-based pre-trained models, but transferring representations learned from natural images to medical images is not optimal and can deteriorate the detection performance in medical domain [12].

Self-supervised pre-training methods that learn auxiliary

pretext tasks [26]–[31] have been shown to produce effective representations for UAD in general computer vision tasks [26]–[28], [32]. However, their application to medical image analysis UAD problems needs to be further investigated because it is unclear how to design effective pretext tasks that can simulate anomalies in medical images. Previous UAD methods relied on self-supervised pretext tasks based on the prediction of geometric transformations [26]–[28] or contrastive learning using standard data augmentation techniques (e.g., scaling, cropping, etc.) [29], [30]. These pretext tasks are not specifically related to the detection of anomalies in medical images, so they may even degrade the detection accuracy of downstream UAD methods [33]. Recently, a self-supervised training that simulates anomalous lesions was proposed [34], but that paper does not show if the method generalises beyond the specific problem of multiple-sclerosis lesion change detection.

We recently introduced the constrained contrastive distribution (CCD) method [12], which is a UAD-oriented self-supervised pre-training method that adapts contrastive learning and two pretext tasks to image anomaly detection. The representations of normal and strongly augmented images (e.g., with random permutations) are pre-trained by CCD to be far apart, where the assumption is that the strongly augmented images can resemble some types of abnormal images, so CCD is enforced to learn discriminative normal representations by contrastive learning. An important contribution of CCD is that it can be applied to any downstream UAD methods to produce SOTA results in popular benchmarks [12]. Although effective, the strong augmentations do not produce realistic synthetic medical image anomalies, which can challenge the training of the downstream UAD approaches. Furthermore, the contrastive loss used by CCD separates samples with weak augmentations from samples of different images or samples with strong augmentations, without discriminating different types of strong augmentation. This does not explicitly force centres around different types of strong augmentation, leading to large variation of features within each type of augmentation that hinders the subsequent anomaly detection and segmentation performance.

In this paper, we propose Multi-centred Strong Augmentation via Contrastive Learning (MSACL), a new self-supervised pre-training method trained exclusively with normal training images, and designed to learn effective image representations for different types of downstream UAD methods. We summarise our contributions as follows:

- Our MSACL extends our previously proposed CCD approach [12] by mapping the distribution of weakly augmented samples away from strong augmented samples and sub-dividing the distribution of these strong augmented samples into several clusters/centres, depending on the type of the strong augmentation. Fundamentally, this contribution transforms the traditional UAD one-class problem into a multi-class classification problem with the objective to improve the effectiveness of the image representations for downstream UAD methods.
- We introduce a new strong data augmentation method named MedMix designed for the detection and segmentation of lesions. MedMix cuts image patches from normal images and pastes them to random locations of other normal images to produce realistic synthetic

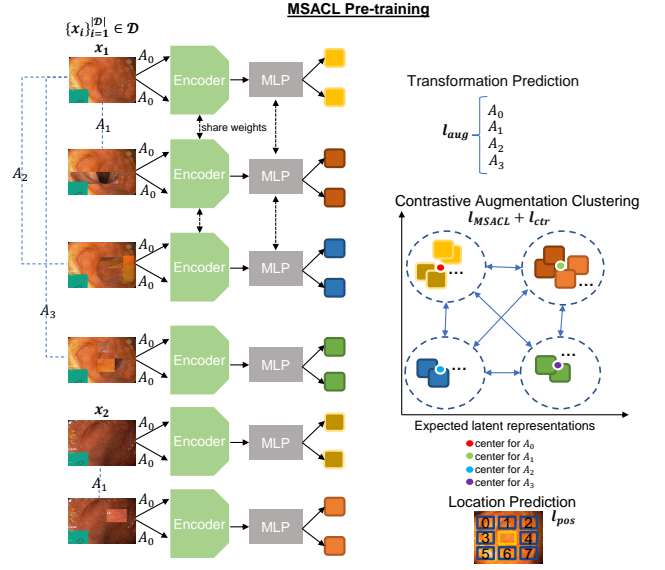


**Fig. 1:** Our proposed self-supervised pre-training method MSACL. It distinguishes images that suffered weak augmentations (set  $\mathcal{A}_0$ ) from images that suffered different types of strong augmentations (sets  $\{\mathcal{A}_i\}_{i=1}^3$ ) using a constrained contrastive learning that trains a multi-class classification problem of four classes. The different types of strong augmentations are produced by MedMix that introduces a varying number of fake lesions in the training images by cutting patches from normal images, altering them with random color jittering, Gaussian noise and non-linear intensity transformations, and pasting them to normal training images. More details of MSACL are presented in Section II-A.

lesions. Learning to discriminate such synthetic anomalous images improves the ability of the model to detect and localise real anomalies. To improve the realism of the synthetic abnormal lesions, we further apply random colour jittering, Gaussian noise and non-linear intensity transformations to the cut-and-paste patches.

We empirically show that our MSACL improves the performance of SOTA predictive and generative anomaly detectors, represented by PaDiM [35] and IGD [13], respectively. Extensive experimental results on four different health screening medical imaging benchmarks, namely, colonoscopy images from two datasets [18], [36], fundus images for glaucoma detection [37] and Covid-19 chest X-ray dataset [38] show that our proposed self-supervised pre-training MSACL can be used to fine-tune diverse SOTA UAD methods to improve their accuracy in detecting and segmenting lesions from medical images.

## II. METHOD

In this section, we introduce the proposed MSACL pre-training approach depicted in Figure 1. Given a training medical image dataset  $\mathcal{D} = \{x_i\}_{i=1}^D$ , with all images assumed to be from the normal class and  $x \in \mathcal{X} \subset \mathbb{R}^{H \times W \times C}$ , our learning strategy involves two stages: 1) the self-supervised pre-training to learn an encoding network  $f_\theta : \mathcal{X} \rightarrow \mathcal{Z}$  (with  $\mathcal{Z} \subset \mathbb{R}^Z$ ), and 2) the fine-tuning of an anomaly detector

or segmentation model built from the pre-trained encoding network  $f_\theta(\cdot)$ . The approach is evaluated on a testing set  $\mathcal{T} = \{(\mathbf{x}, y, \mathbf{m})_i\}_{i=1}^{|\mathcal{T}|}$ , where  $y \in \mathcal{Y} = \{\text{normal}, \text{abnormal}\}$ , and  $\mathbf{m} \in \mathcal{M} \subset \{0, 1\}^{H \times W \times C}$  denotes the segmentation mask of the lesion in the image  $\mathbf{x}$ .

### A. Multi-centred Strong Augmentation

The gist of our proposed MSACL lies in the idea of discriminating the distribution of weakly augmented samples from the distributions of different types of strongly augmented samples produced by our MedMix. As explained below in Section II-B, and shown in Figure 2, MedMix is designed to produce normal images from weak augmentations, and different types of abnormal images that contain a varying number of synthetic anomalies per image. Therefore, our learning objective discriminates not only between normal and abnormal images, but also between the different classes of abnormal images. Our motivation is that this multi-class optimisation can mitigate the catastrophic collapse issue, usually seen in predictive-based anomaly detection methods, where image representations collapse to a single vector that represents the normal images [22], [39]. To this end, our proposed loss is defined as:

$$\ell(\mathcal{D}; \theta, \beta, \gamma) = \ell_{ctr}(\mathcal{D}; \theta) + \ell_{MSACL}(\mathcal{D}; \theta) + \ell_{aug}(\mathcal{D}; \beta) + \ell_{pos}(\mathcal{D}; \gamma), \quad (1)$$

where  $\ell_{ctr}(\cdot)$  denotes the new distribution multi-centring loss,  $\ell_{MSACL}(\cdot)$  represents the new MSACL loss,  $\ell_{aug}(\cdot)$  and  $\ell_{pos}(\cdot)$  are the pretext learning losses to constrain optimisation [12], and  $\theta$ ,  $\beta$  and  $\gamma$  are trainable parameters. The loss terms in (1) rely on **weak data augmentation distribution**, denoted by  $\mathcal{A}_0$ , and  $|\mathcal{A}|$  **strong data augmentation distributions**, represented by  $\{\mathcal{A}_n\}_{n=1}^{|\mathcal{A}|}$ , each denoting a different type of augmentation. From each of these distributions, we can sample augmentation functions  $a: \mathcal{X} \rightarrow \mathcal{X}$ .

The multi-centring loss in (1) depends on the estimation of the mean representation for each strong augmentation distribution, computed as

$$\mathbf{c}_n = \mathbb{E}_{\mathbf{x} \in \mathcal{D}, a \sim \mathcal{A}_n} [f_\theta(a(\mathbf{x}))], \quad (2)$$

where  $n \in \{0, \dots, |\mathcal{A}|\}$ , with  $\mathbf{c}_n$  being the mean representation of the training data augmented by the functions sampled from  $\mathcal{A}_n$ , for  $n \in \{0, \dots, |\mathcal{A}|\}$ . Note that these mean representations are computed at the beginning of the training and frozen for the rest of the training. The distribution multi-centring loss is then defined as:

$$\ell_{ctr}(\mathcal{D}; \theta) = \mathbb{E}_{\mathbf{x} \in \mathcal{D}, n \in \{0, \dots, |\mathcal{A}|\}, a \sim \mathcal{A}_n} \|f_\theta(a(\mathbf{x})) - \mathbf{c}_n\|^2, \quad (3)$$

which is designed to pull the representations of strong augmented samples towards the mean representations defined in (2).

Standard contrastive learning [12], [29], [30] aims to decrease the cosine similarity between positive (represented by two different augmentations of the same image) and negative samples (denoted by different images). Such objective results in a method that approximates augmented samples of the same image and repels different images. We adapt this objective to anomaly detection by re-formulating contrastive learning such that it approximates weakly augmented samples from the same image and repels not only different images, but

also different types of strongly augmented samples from the same image [12]. An innovative aspect of our contrastive learning formulation is that we subtract the centre  $\mathbf{c}_n$  from the feature produced by  $f_\theta(a(\mathbf{x}))$  to allow a clustering not only in the Euclidean space (with the samples close to their mean representations  $\mathbf{c}_n$ ), but also in the hyper-sphere around the mean representations  $\mathbf{c}_n$ . Such re-formulated contrastive learning, combined with the multi-centring loss (3), results in a loss that produces multiple clusters, where cluster  $n = 0$  contains the normal images and the others, denoted by  $n \in \{1, \dots, |\mathcal{A}|\}$ , have the synthetic abnormal images. Our proposed MSACL loss is defined as:

$$\ell_{MSACL}(\mathcal{D}; \theta) = \mathbb{E}_{\mathbf{x} \in \mathcal{D}, n \in \{0, \dots, |\mathcal{A}|\}, l \in \{0, 1\}} [\ell_{MSACL}^x(\mathbf{x}^{(n,l)}, \mathcal{D}; \theta)] \quad (4)$$

where  $\mathbf{x}^{(n,l)} = a(\mathbf{x}^{(n)})$  represents one of two (indexed by  $l \in \{0, 1\}$ ) augmented data obtained from the application of a weak augmentation  $a \sim \mathcal{A}_0$  on a strongly augmented data denoted by  $\mathbf{x}^{(n)} = a(\mathbf{x})$  with  $a \sim \mathcal{A}_n$ . In (4), we have:

$$\begin{aligned} \ell_{MSACL}^x(\mathbf{x}^{(n,l)}, \mathcal{D}; \theta) = & -\log \frac{\exp \left[ \frac{1}{\tau} \tilde{f}_\theta(\mathbf{x}^{(n,l)})^\top \tilde{f}_\theta(\mathbf{x}^{(n, (l+1) \bmod 2}) \right]}{\sum_{\substack{\mathbf{x}_j \in \mathcal{D} \\ m \in \{0, \dots, |\mathcal{A}|\} \\ k \in \{0, 1\}}} \mathbb{I}(\mathbf{x}_j^{(m,k)} \neq \mathbf{x}^{(n,l)}) \exp \left[ \kappa(n, m) \tilde{f}_\theta(\mathbf{x}^{(n,l)})^\top \tilde{f}_\theta(\mathbf{x}_j^{(m,k)}) \right]}, \end{aligned} \quad (5)$$

where  $\mathbb{I}(\cdot)$  denotes an indicator function,  $\mathbf{x}_j^{(m,k)}$  is defined similarly as  $\mathbf{x}^{(n,l)}$  in (4),  $m \in \{0, \dots, |\mathcal{A}|\}$  indexes the set of strong augmentations, and  $k \in \{0, 1\}$  indexes one of the two weak augmentations applied to the strongly augmented image. To constrain the strongly augmented data representations in (4), our MSACL loss minimises the distance between samples centred by their representation means computed as:

$$\tilde{f}_\theta(\mathbf{x}^{(n,l)}) = \frac{f_\theta(\mathbf{x}^{(n,l)}) - \mathbf{c}_n}{\|f_\theta(\mathbf{x}^{(n,l)}) - \mathbf{c}_n\|_2}, \quad (6)$$

where  $\mathbf{c}_n$  is defined in (2). Also in (4) to map the representations from the same distribution into a denser region of the hyper-sphere, we use a temperature calibration strategy defined as:

$$\kappa(n, m) = \begin{cases} 1/(\alpha\tau) & , \text{ if } n = m \\ 1/\tau & , \text{ otherwise } \end{cases}, \quad (7)$$

where  $\alpha$  is a scaling factor that controls the shrinkage level of the temperature  $\tau$ . Note that in (7), when two images are produced by the same strong augmentation distributions (i.e., when  $n = m$ ), they will be repelled by a smaller amount than when the images are produced by different strong augmentation distributions. Putting all together, the loss in (4) clusters the image representations into hyper-spheres and regions within the hyper-spheres, where each hyper-sphere and region represent a different type of augmentation.

We further constrain the training in (1) with a self-supervised classification constraint  $\ell_{cla}(\cdot)$  that enforces the model to classify the strong augmentation function (see Figure 1):

$$\ell_{cla}(\mathcal{D}; \beta) = -\mathbb{E}_{\mathbf{x} \in \mathcal{D}, n \in \{0, \dots, |\mathcal{A}|\}, a \sim \mathcal{A}_n} [\log \mathbf{a}_n^\top f_\beta(f_\theta(a(\mathbf{x})))] \quad (8)$$

where  $f_\beta: \mathcal{Z} \rightarrow [0, 1]^{|\mathcal{A}|}$  is a fully-connected (FC) layer, and  $\mathbf{a}_n \in \{0, 1\}^{|\mathcal{A}|}$  is a one-hot vector representing the strong



augmentation distribution (i.e.,  $\mathbf{a}_n(j) = 1$  for  $j = n$ , and  $\mathbf{a}_n(j) = 0$  for  $j \neq n$ ).

The final constraint in (1) is based on the relative patch location from the centre of the training image and is adapted for local patches (see Figure 1). This constraint is added to learn positional and texture characteristics of the image in a self-supervised manner. Inspired by [40], the positional constraint predicts the relative position of the paired image patches, with its loss defined as

$$\ell_{pos}(\mathcal{D}; \gamma) = -\mathbb{E}_{\{\mathbf{x}_{\omega_1}, \mathbf{x}_{\omega_2}\} \sim \mathbf{x} \in \mathcal{D}} [\log \mathbf{p}^\top f_\gamma(f_\theta(\mathbf{x}_{\omega_1}), f_\theta(\mathbf{x}_{\omega_2}))], \quad (9)$$

where  $\mathbf{x}_{\omega_1}$  is a randomly selected fixed-size image patch from  $\mathbf{x}$ ,  $\mathbf{x}_{\omega_2}$  is another image patch from one of its eight neighbouring patches (as shown in ‘patch location prediction’ in Figure 1),  $\omega_1, \omega_2 \in \Omega$  represents indices to the image lattice,  $f_\gamma : \mathcal{Z} \times \mathcal{Z} \rightarrow [0, 1]^8$ , and  $\mathbf{p} = \{0, 1\}^8$  is a one-hot encoding of the patch location.

Overall, the constraints in (8) and (9) are designed to improve the discriminatyn between normal and abnormal samples. This is shown empirically in the quantitative results in Section III and the t-SNE results in Figure 7.

### B. MedMix Augmentation

Our MedMix augmentation is designed to augment images in such way that they resemble images containing medical anomalies (e.g., lesions or tumours). This improves upon our previous work [12] that relied on strong augmentations (i.e., permutations, rotations) that do not resemble anomalies in medical images, which can yield poor detection performance by downstream UAD methods. We realise that anomalies in different medical domains (e.g., glaucoma and colon polyps) can be visually different, but a commonality among anomalies is that they are usually represented by an unusual growth of abnormal tissue. Hence, we propose the MedMix augmentation that simulates unusual growth of abnormal tissue with a strong augmentation that “constructs” abnormal lesions by cutting and pasting (from and to normal images) small and visually deformed patches. This visual deformation is achieved by applying other transformations to patches, such as colour jittering, Gaussian noise and non-linear intensity transformations. This approach is inspired by cutmix [41], where our contribution over cutmix is the intensification of the change present in the cropped patches by the appearance transformations above. These transformations are designed to encourage the model to learn abnormalities in terms of localised image appearance, structure, texture and colour.

In practice, we design  $|\mathcal{A}| = 4$  strong augmentation distributions, where  $\mathcal{A}_n$  includes  $n \in \{0, \dots, 3\}$  abnormalities in the image, which means that  $\mathcal{A}_0$  denotes the normal image distribution and  $\mathcal{A}_{n \in \{1, 2, 3\}}$  represent the abnormal image distributions, containing  $\{1, 2, 3\}$  anomalous regions. Therefore, our loss targets distinguishing different number of MedMix augmentations, as shown in Figure 2.

### C. Anomaly Detection and Segmentation

After pre-training the model  $f_\theta(\cdot)$  with our proposed MSACL from Section II-A and II-B, we can fine-tune it with a state-of-the-art unsupervised anomaly detector, such as IGD [13] or PaDiM [35]. Those two methods use the same

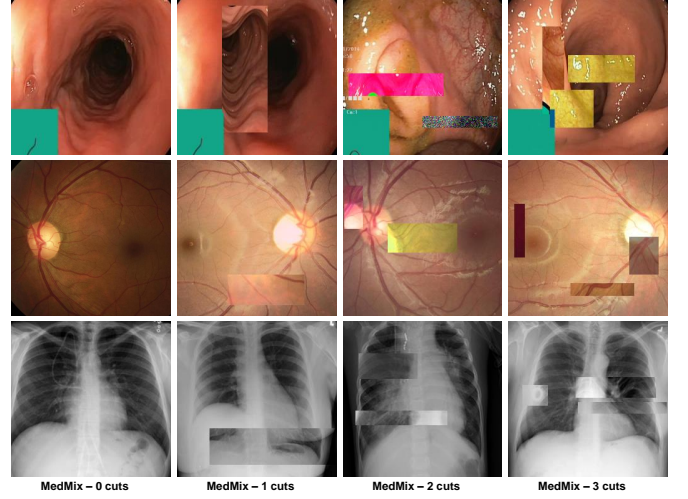


Fig. 2: Examples of our MedMix data augmentation, showing augmentation  $\mathcal{A}_0$  containing zero synthetic anomalies (leftmost column) and increasingly stronger augmentations  $\{\mathcal{A}_n\}_{n=1}^3$  (second to fourth columns) with different number of synthetic anomalies (from one to three).

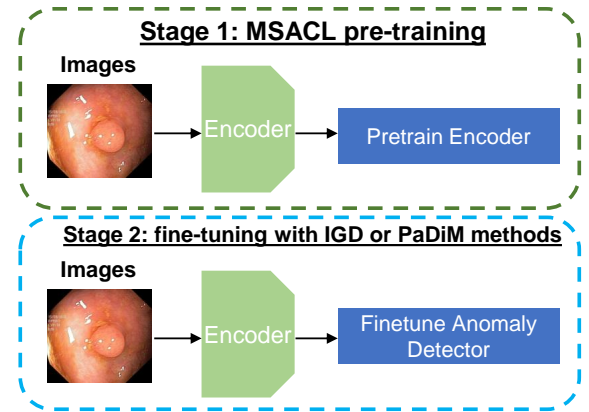


Fig. 3: Our proposed two-stage anomaly detection/segmentation framework.

training set  $\mathcal{D}$ , as used by MSACL, containing only normal images from healthy patients.

IGD [13] combines three loss functions: 1) two reconstruction losses based on local and global multi-scale structural similarity index measure (MS-SSIM) [42] and mean absolute error (MAE) to train the encoder  $f_\theta : \mathcal{X} \rightarrow \mathcal{Z}$  and decoder  $g_\phi : \mathcal{Z} \rightarrow \mathcal{X}$ , 2) a regularisation loss to train adversarial interpolations from the encoder [43], and 3) an anomaly classification loss to train  $h_\psi : \mathcal{Z} \rightarrow [0, 1]$ . The anomaly detection score of image  $\mathbf{x}$  is defined by

$$s_{IGD}(\mathbf{x}) = \xi \ell_{rec}(\mathbf{x}, \tilde{\mathbf{x}}) + (1 - \xi)(1 - h_\psi(f_\theta(\mathbf{x}))), \quad (10)$$

where  $\tilde{\mathbf{x}} = g_\phi(f_\theta(\mathbf{x}))$ ,  $h_\psi(\cdot)$  returns the likelihood that  $\mathbf{x}$  belongs to the normal class,  $\xi \in [0, 1]$  is a hyper-parameter, and

$$\ell_{rec}(\mathbf{x}, \tilde{\mathbf{x}}) = \rho \|\mathbf{x} - \tilde{\mathbf{x}}\|_1 + (1 - \rho)(1 - (\nu m_G(\mathbf{x}, \tilde{\mathbf{x}}) + (1 - \nu)m_L(\mathbf{x}, \tilde{\mathbf{x}}))), \quad (11)$$

with  $\rho, \nu \in [0, 1]$ ,  $m_G(\cdot)$  and  $m_L(\cdot)$  denoting the global and local MS-SSIM scores from the global and local models, respectively [13]. Anomaly segmentation uses (10) to compute  $s_{IGD}(\mathbf{x}_\omega)$ ,  $\forall \omega \in \Omega$  using global and local models, where  $\mathbf{x}_\omega \in \mathbb{R}^{H \times W \times C}$  is an image patch. This forms a heatmap, where large values of  $s_{IGD}(\cdot)$  denote anomalous regions. The final heatmap is formed by summing up the global and local heatmaps.

PaDiM [35] utilises the multi-layer features from the pre-trained network  $f_\theta(\cdot)$  to learn a position dependent multi-variate Gaussian distribution of normal image patches. Training uses samples collected from the concatenation of the multi-layer features from each patch position  $\omega \in \Omega$  to learn the mean and covariance of the Gaussian model denoted by  $\mathcal{N}(\mu_\omega, \Sigma_\omega)$  [35]. Anomaly detection is based on the Mahalanobis distance between the concatenated testing patch feature  $\mathbf{x}_\omega$  and the learned Gaussian distribution  $\mathcal{N}(\mu_\omega, \Sigma_\omega)$  at that patch position  $\omega \in \Omega$  to provide a score of each patch position [35]. In particular, anomaly segmentation is inferred using the following anomaly score map:

$$s_{PaDiM}(\mathbf{x}_\omega) = \sqrt{(\mathbf{x}_\omega - \mu_\omega)^\top \Sigma_\omega^{-1} (\mathbf{x}_\omega - \mu_\omega)}, \quad (12)$$

and the final score of the whole image  $\mathbf{x}$  is defined as:  $s_{PaDiM}(\mathbf{x}) = \max_{\omega \in \Omega} s_{PaDiM}(\mathbf{x}_\omega)$ .

### III. EXPERIMENTS

#### A. Datasets

We test our self-supervised pre-training MSACL on four health screening datasets, where we run experiments for both anomaly detection and localisation. For the anomaly detection and localisation, the datasets are: the colonoscopy images of Hyper-Kvasir dataset [36], and the glaucoma dataset using fundus images [37]. For the anomaly detection, the datasets are: the colonoscopy dataset [18], and Covid-19 chest ray dataset [38] – these two datasets do not have lesion segmentation annotations, so we test anomaly detection only.

**Hyper-Kvasir** is a large multi-class public gastrointestinal imaging dataset [36]. The data were collected from the gastroscopy and colonoscopy procedures from Baerum Hospital in Norway. All labels were produced by experienced clinicians. The dataset contains 110,079 images from abnormal (i.e., unhealthy) and normal (i.e., healthy) patients, where 10,662 of those images have been labelled. We use a subset of the normal (i.e., healthy) images from the dataset for training. Specifically, 2,100 images from ‘cecum’, ‘ileum’ and ‘bbsps-2-3’ are selected as normal, from which we use 1,600 for training and 500 for testing. We also take 1,000 abnormal images and their segmentation masks of polyps to be used exclusively for testing, with the size of  $300 \times 300$ .

**LAG** is a large scale fundus image dataset for glaucoma diagnosis [37], containing 4,854 fundus images with 1,711 positive glaucoma scans and 3,143 negative glaucoma scans. For the experiments, we use 2,343 normal (negative glaucoma) images for training, and 800 normal images and 1,711 abnormal images with positive glaucoma with annotated attention maps by ophthalmologists in glaucoma diagnosis, with the size of  $500 \times 500$ . The attention maps is based on an alternative method for eye tracking, in which the maps are used by the ophthalmologists to explore the region of interest for glaucoma diagnosis [37].

**Liu et al.’s colonoscopy dataset** is a colonoscopy image dataset with 18 colonoscopy videos from 15 patients [18]. The training set contains 13,250 normal (healthy) images without any polyps, and the testing set contains 967 images, with 290 abnormal images with polyps and 677 normal (healthy) images without polyps, with the size of  $64 \times 64$ .

**Covid-X** [38] has a training set with 1,670 COVID-19 positive chest x-ray images, and 13,794 COVID-19 negative chest X-ray images. The test set contains 400 chest X-rays, consisting of 200 positive and 200 negative images. We train the methods with the 13,794 COVID-19 negative chest X-ray training images and test on the 400 chest X-ray images, with the size of  $299 \times 299$ .

#### B. Implementation Details

For the proposed MSACL pre-training, we use Resnet18 [44] as the backbone architecture for the encoder  $f_\theta(\mathbf{x})$ , and similarly to previous works [29], [45], we add an MLP to this backbone as the projection head for the contrastive learning, which outputs features in  $\mathcal{Z}$  of size 128. All images from the Hyper-Kvasir [36], LAG [37] and Covid-X [38] datasets are resized to  $256 \times 256$  pixels. For the Liu et al.’s colonoscopy dataset [18], images are resized to  $64 \times 64$  pixels. The batch size is set to 32 and learning rate to 0.01 for the self-supervised pre-training on all datasets. The model is trained using stochastic gradient descent (SGD) optimiser with momentum.

We investigate the impact of different strong augmentations in  $\mathcal{A}_n$ , including rotation, permutation, cutout, Gaussian noise and our proposed MedMix. For MedMix patches, we randomly apply colour jittering, Gaussian noise and non-linear intensity transformations (i.e., fisheye and horizontal wave transformations). The weak augmentations in  $\mathcal{A}_0$  are the same as in SimCLR [29], namely: colour jittering, random grey scale, crop, resize, and Gaussian blur.

The model pre-trained with MSACL is fine-tuned with IGD [13] or PaDiM [35]. For IGD [13], we pre-train the global and local models (see Figure 1), where the patch position prediction loss in Eq. 9 is only fine-tuned for the local model. For PaDiM [35], we pre-train the global model and use it to fine-tune the anomaly detection and segmentation models. For the training of IGD [13] and PaDiM [35], we use the hyper-parameters suggested by the respective papers. In our experiments, the local map for IGD is obtained by considering each  $32 \times 32$ -pixel patch as an instance and apply our proposed self-supervised learning to it. The global map for IGD is computed based on the whole image sized as  $256 \times 256$  pixels for Hyper-Kvasir, LAG and Covid-X datasets. For Liu et al.’s colonoscopy dataset, we only train the model globally with the image size  $64 \times 64$ . For the auto-encoder in IGD, we use the setup suggested in [13], where the global model is trained with images of size  $256 \times 256$  pixels or  $64 \times 64$  for Liu et al.’s colonoscopy dataset, and the local model is trained with image patches of size  $32 \times 32$ . For PaDiM [35], we only use the default setup in their work and compute the segmentation mask based on the images of size  $256 \times 256$  pixels for Hyper-Kvasir, LAG and Covid-X datasets, and  $64 \times 64$  for Liu et al.’s colonoscopy dataset.

Methods	AUC	Specificity	Sensitivity	Accuracy
DAE [47]	0.705	0.522	0.756	0.693
OCGAN [48]	0.813	0.691	0.811	0.795
f-AnoGAN [15]	0.907	0.846	0.915	0.883
ADGAN [3]	0.913	0.879	0.946	0.893
MS-SSIM [13]	0.917	0.857	0.925	0.912
PaDiM [35]	0.943	0.846	0.929	0.898
CCD - PaDiM	0.978	0.923	0.961	0.967
<b>MSACL - PaDiM</b>	<b>0.996</b>	<b>0.966</b>	<b>0.981</b>	<b>0.983</b>
IGD [13]	0.939	0.858	0.913	0.906
CCD - IGD	0.972	0.934	0.947	0.956
<b>MSACL - IGD</b>	<b>0.995</b>	<b>0.947</b>	<b>0.965</b>	<b>0.972</b>

**TABLE I: Anomaly detection testing results on Hyper-Kvasir** in terms of AUC, Specificity, Sensitivity and Accuracy. Best results are highlighted.

### C. Evaluation Measures

The anomaly detection performance is quantitatively assessed by the area under the ROC curve (AUROC), specificity, sensitivity and accuracy. AUROC has been used to evaluate the performance of anomaly detection. Sensitivity and specificity reflect the percentage of positives and negatives that are correctly detected. Accuracy shows the overall performance of correctly detected samples for both positive and negative images, where the threshold of classifying positive/negative samples is estimated with a small validation set that contains 50 normal and 50 abnormal images that randomly sampled from the testing set. Note that the validation set is only used for threshold estimation.

For anomaly segmentation, the performance is measured by Intersection over Union (IoU), Dice score (Dice) and the per-region-overlap score (Pro-score) [46]. IoU is computed by dividing the intersection by the union between the predicted segmentation and the ground truth mask. Dice also takes the predicted segmentation and the ground truth mask and divides two times their intersection by their sum. Pro-score weights the ground-truth masks of different sizes equally [46] to verify if both large and small abnormal lesions are accurately segmented.

### D. Lesion Detection Results

1) *Detection Results on Hyper-Kvasir*: In Table I, we show the results of anomaly detection on Hyper-Kvasir dataset, where we present results from baseline UAD methods, including OCGAN [48], f-AnoGAN [15], ADGAN [18], and deep autoencoder [47] and its variant with MS-SSIM loss [13]. As discussed in Section II-C, we choose IGD [13] and PaDiM [35] as the anomaly detector for evaluating our proposed MSACL pre-training approach and compare it with our previously proposed CCD pre-training approach [12] to fine-tune IGD and PaDiM.

Comparing with the baseline UAD methods, the performance of PaDiM and IGD are improved using our MSACL pre-trained encoder by around 5% and 6% AUC, which achieves SOTA anomaly detection AUC results of 99.6% and 99.5%, respectively, on Hyper-Kvasir. Comparing with our previously proposed CCD pre-training [12], our proposed MSACL pre-training improves the performance by 2.3% and 1.8% for PaDiM and IGD. This shows that our proposed MedMix and MSACL loss improve the generalisation aty of the fine-tuning stage for anomaly detection and produce better constrained feature space of normal samples. Moreover,

Methods	AUC	Specificity	Sensitivity	Accuracy
MS-SSIM [13]	0.823	0.257	0.937	0.774
f-AnoGAN [15]	0.778	0.565	0.899	0.763
PaDiM [35]	0.688	0.314	0.809	0.673
CCD - PaDiM	0.728	0.429	0.779	0.694
<b>MSACL - PaDiM</b>	<b>0.761</b>	<b>0.466</b>	<b>0.877</b>	<b>0.753</b>
IGD [13]	0.796	0.396	0.958	0.805
CCD - IGD	0.874	<b>0.572</b>	0.944	0.875
<b>MSACL - IGD</b>	<b>0.908</b>	0.531	<b>0.979</b>	<b>0.884</b>

**TABLE II: Anomaly detection testing results on LAG** in terms of AUC, Specificity, Sensitivity, Precision and Recall. Best results are highlighted.

Methods	AUC	Specificity	Sensitivity	Accuracy
DAE [47]	0.629*	0.733*	0.554*	0.597*
OCGAN [48]	0.592*	0.716*	0.534*	0.624*
ADGAN [3]	0.730*	0.852*	0.496*	0.713*
f-AnoGAN [15]	0.735	0.865	0.579	0.694
PaDiM [35]	0.741	0.851	0.738	0.751
CCD - PaDiM	0.789	0.946	0.792	0.767
<b>MSACL - PaDiM</b>	<b>0.814</b>	<b>0.973</b>	<b>0.725</b>	<b>0.803</b>
IGD [13]	0.787	0.914	0.596	0.743
CCD - IGD	0.837	0.985	0.774	0.815
<b>MSACL - IGD</b>	<b>0.851</b>	<b>0.986</b>	<b>0.792</b>	<b>0.829</b>

**TABLE III: Anomaly detection testing results on Liu et al.'s colonoscopy** in terms of AUC, Specificity, Sensitivity and Accuracy. \* indicates that the model does not use ImageNet pre-training. Best results are highlighted.

achieving SOTA results on two different types of anomaly detectors suggests that our self-supervised pre-training can produce good representations for both generative and predictive anomaly detectors. OCGAN [48] constrains the latent space based on two discriminators to force the latent representations of normal data to fall at a bounded area. f-AnoGAN [15] uses an encoder to extract the feature representations of a input image and use a GAN to reconstruct it. ADGAN [3] uses two generators and two discriminators to produce realistic reconstruction of normal samples. These three methods achieve 81.3%, 90.7% and 91.3% AUC on Hyper-Kvasir, respectively, which are well below our self-supervised MSACL pre-training with IGD and PaDiM. Also, PaDiM with our MSACL pre-training can achieve the SOTA results of 96.6% specificity, 98.1% sensitivity and 98.3% accuracy. It improves the previous PaDiM using CCD pre-training by 4.3%, 2% and 1.6% in terms of these three evaluation measures. Further, PaDiM pre-trained with MSACL significantly outperforms the PaDiM pre-trained with ImageNet [35] by 12%, 5.2% and 8.5% in terms of these three evaluation measures.

2) *Detection Results on LAG*: We evaluate the performance of our MSACL pre-training on LAG dataset and show results on Table II. Our MSACL pre-training improves PaDiM and IGD AUCs by 7.3% and 11.2%, compared with their ImageNet pre-trained model, where the MSACL pre-trained IGD achieves the SOTA results of 90.8% AUC, 97.9% sensitivity and 88.4% accuracy. Comparing with our previous CCD pre-trained PaDiM and IGD [12], our proposed MSACL pre-trained PaDiM and IGD surpass them by 3.3% and 3.4% in terms of AUC. The MS-SSIM autoencoder [13] and f-AnoGAN [15] baselines achieve 82.3% and 77.8% AUC, respectively, which are significantly inferior compared with our MSACL pre-trained methods. For LAG, the glaucoma features are often subtle and easy to neglect, so IGD with both reconstruction and anomaly classification constraints can



Methods	AUC	Specificity	Sensitivity	Accuracy
PaDiM [35]	0.614	0.753	0.318	0.559
CCD - PaDiM	0.632	0.673	0.569	0.616
<b>MSACL - PaDiM</b>	0.658	0.749	0.467	0.615
IGD [13]	0.699	<b>0.885</b>	0.490	0.688
CCD - IGD	0.746	0.851	0.595	0.722
<b>MSACL - IGD</b>	<b>0.872</b>	0.863	<b>0.775</b>	<b>0.813</b>

**TABLE IV:** Anomaly detection testing results on **Covid-X** in terms of AUC, Specificity, Sensitivity and Accuracy, respectively. Best results are highlighted.

generally perform better than PaDiM variants.

### 3) Detection Results on Liu *et al.*'s colonoscopy dataset:

We further test our approach on Liu *et al.*'s colonoscopy dataset [3], as shown in Table III. Similarly to the previous results, our MSACL pre-trained PaDiM improves the ImageNet pre-trained PaDiM by 7.3% AUC, and CCD pre-trained PaDiM by 2.5% of AUC. The IGD with the MSACL pre-trained encoder achieves the SOTA result of 85.1% AUC, surpassing the previous CCD and ImageNet pre-trained IGD by 1.4% and 6.4% AUC, respectively.

Compared with other UAD approaches, such as f-AnoGAN, ADGAN and OCGAN that achieve 73.5%, 73% and 59.2% AUC, our MSACL pre-trained IGD and PaDiM produce substantially better results. The gap between PaDiM and IGD may be due to the low resolution of the images in this dataset, which hinders the PaDiM performance that requires dense intermediate feature maps. The additional results of the MSACL pre-trained IGD are specificity of 98.6%, sensitivity of 79.2%, and accuracy of 82.9%, which demonstrate the robustness of our proposed model.

**4) Detection Results on Covid-X:** Our MSACL pre-trained PaDiM and IGD methods achieve 65.8% and 87.2% AUC on the Covid-X dataset, significantly surpassing their ImageNet pre-trained by 4.4% and 17.2% AUC, and CCD pre-trained by 2.6% and 12.6% AUC. The small abnormal lesions in chest X-ray images are hard to detect, so the generative-based anomaly detector IGD can learn more effectively the fine-grained appearances of normal images, leading to better ability to detect unseen anomalous regions during testing with the SOTA results of 87.2% AUC, 77.5% of sensitivity and 81.3% of accuracy. The MSACL pre-trained IGD achieves 86.3% specificity, which is competitive with the result from IGD pre-trained with ImageNet. It can also be observed that our MSACL pre-trained PaDiM and IGD improve sensitivity by 14.9% and 28.5%, when compared to the ImageNet pre-trained PaDiM and IGD.

**5) Variaty in the Results:** We show on Table V the standard deviation computed from the AUC, specificity, sensitivity and accuracy results of five different trainings based on different model initialisation of the MSACL pre-trained PaDiM detector. These results in Table V should be studied together with the Tables I, II, IV. In general, we conclude that the differences between the methods described in the sections above can be considered significant in most cases given that the standard deviation only varies from 0.5% to 1.5%.

## E. Lesion Segmentation Results

**1) Segmentation results on Hyper-Kvasir:** We demonstrate the anomaly segmentation performance on Hyper-Kvasir on

Dataset	AUC	Specificity	Sensitivity	Accuracy
Hyper-Kvasir [36]	0.0084	0.0079	0.0127	0.0036
LAG [37]	0.0163	0.0085	0.0105	0.0121
Covid-X [38]	0.0107	0.0149	0.0092	0.0171

**TABLE V:** The standard deviation of five-run experimental results on the Hyper-Kvasir, LAG and Covid-X based on the MSACL pre-trained PaDiM anomaly detector. This results should be studied together with the results shown in Tables I, II, IV.

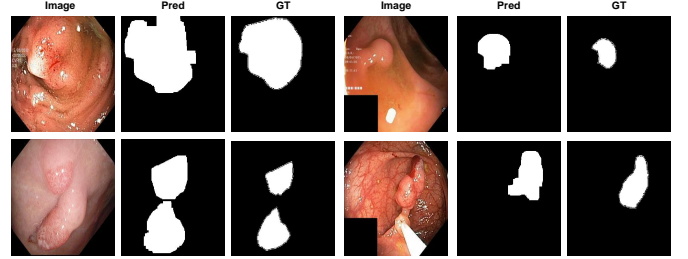


**Fig. 4:** Segmentation of four abnormal images from Hyper Kvasir [37], with their predictions (Pred) and ground truth annotations (GT), using PaDiM with MSACL pre-training.

Table VI. Following [12], we randomly sample 100 abnormal images from the test set and compute the mean segmentation performance over five different such groups of 100 images. Compared to the current SOTA UAD segmentation method, CAVGA- $R_u$  [19], IGD and PaDiM pre-trained with our previous CCD is more than 3% better in terms of IoU. The proposed MSACL pre-training improves the IGD and PaDiM by 1.2% and 2.8% IoU compared with the CCD pre-training, and 8.1% and 6.4% IoU with respect to the ImageNet pre-training, respectively. In addition, our MSACL pre-trained PaDiM shows the SOTA result of 40.6% IoU and 55.4% Dice, demonstrating the effectiveness of our MSACL approach for abnormal lesion segmentation. The CCD version of PaDiM achieves the SOTA result of 88.1% Pro-score.

We also compare our results to fully supervised methods [49]–[52] to assess the accuracy gap when suppressing supervision from abnormal data. The fully supervised baselines [49]–[52] use 80% of the annotated 1,000 colonoscopy images containing polyps during training, 10% for validation and 10% for testing. We validate the unsupervised approaches using the same number of testing samples, but without using abnormal samples for training. Notice on Table VI that we lose between 30% and 40% IoU and Dice for not using abnormal samples for training.

**2) Segmentation results on LAG:** We further demonstrate the segmentation results on LAG dataset on Table VII. The MSACL pre-trained IGD achieves the SOTA result of 51.6% IoU, 66.7% Dice and 69.3% Pro-score, showing that our model can effectively segment different types of lesions, such as colon polyps or optic disk and cup with Glaucoma. Moreover, PaDiM pre-trained with MSACL improves PaDiM pre-trained with CCD and ImageNet by 1.3% and 4.8% IoU, respectively. Also, PaDiM with MSACL pre-training achieves 64.3% Dice and 62.8% Pro-score, which are comparable to the SOTA results by the MSACL pre-trained IGD.

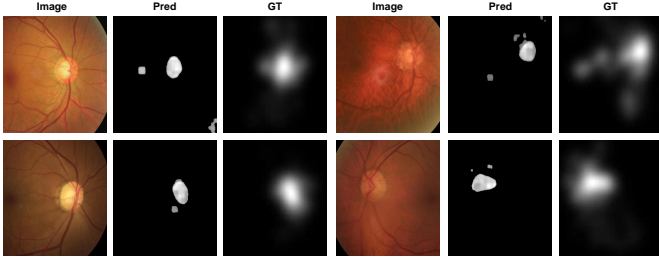


Fig. 5: Segmentation of four abnormal images from LAG [37], with their predictions (Pred) and ground truth attention maps by ophthalmologists in glaucoma diagnosis (GT), using IGD with MSACL pre-training.

Supervision	Methods	IoU	Dice	Pro
Supervised	U-Net [49]	0.746	0.818	-
	U-Net++ [50]	0.743	<b>0.821</b>	-
	ResUNet [51]	<b>0.793</b>	0.813	-
	SFA [52]	0.611	0.723	-
	CAVGA- $R_u$ [19]	0.349	0.465	0.818
Unsupervised	PaDiM [35]	0.341	0.475	0.803
	CCD - PaDiM	0.378	0.497	<b>0.881</b>
	<b>MSACL - PaDiM</b>	<b>0.406</b>	<b>0.554</b>	0.854
	IGD [13]	0.303	0.417	0.794
	CCD - IGD	0.372	0.502	0.865
	<b>MSACL - IGD</b>	0.384	0.521	0.876

TABLE VI: Anomaly segmentation: Mean IoU, Dice and PRO-AUC testing results on **Hyper-Kvasir** on 5 different groups of 100 images with ground truth masks. We show results by fully-supervised methods (top) and unsupervised methods (bottom). Best results for each case are highlighted.

## F. Qualitative Results

1) *Visualisation of predicted segmentation*: The visualisation of polyp segmentation results of PaDiM with MSACL pre-training on Hyper-Kvasir [36] are shown in Figure 4. Notice that our model can effectively segment colon polyps with various sizes and shapes. We also show the segmentation results based on the pixel-level anomaly scores of IGD with MSACL pre-training on the LAG dataset in Figure 5.

2) *Visualisation of predicted anomaly scores*: The visual anomaly detection results of IGD pre-trained with MSACL on the Hyper-Kvasir [36] test set is shown in Figure 6.

3) *Visualisation of t-SNE results*: To validate the effectiveness of our proposed MSACL pre-training, we compare the image representations produced by ImageNet, CCD and MSACL pre-training, using t-SNE on Hyper-Kvasir. The results are shown in Figure 7. The proposed MSACL appears to cluster all the normal data into a well-constrained region of the representation space, where the abnormal data fall outside of this region in relatively distinct three clusters, which appear to represent the three strong augmentations. In contrast, the models pre-trained with ImageNet and CCD produce a poorly clustered normal data that is likely to challenge the training of the downstream UAD method.

## G. Ablation Study

1) *Different components of MSACL pre-training*: We present an ablation study that shows the influence of each step of our proposed MSACL pre-training and PaDiM fine-tuning in

Methods	IoU	Dice	Pro
PaDiM [35]	0.427	0.579	0.596
CCD - PaDiM	0.462	0.612	0.634
<b>MSACL - PaDiM</b>	0.475	0.643	0.628
IGD [13]	0.409	0.539	0.603
CCD - IGD	0.509	0.645	0.677
<b>MSACL - IGD</b>	<b>0.516</b>	<b>0.667</b>	<b>0.693</b>

TABLE VII: Anomaly segmentation: Mean IoU, Dice and Pro-AUC testing results on abnormal samples from **LAG** test set. Best results are highlighted.

CCD [12]	MedMix	$\ell_{MSACL}$	$\kappa(i, k)$	AUC - Hyper	AUC - LAG
✓				0.978	0.728
✓	✓			0.985	0.739
	✓	✓		0.993	0.753
	✓	✓	✓	0.996	0.761

TABLE VIII: Ablation study of the MSACL components on Hyper-Kvasir and LAG, using PaDiM [35] as anomaly detector. Best results are highlighted.

Table VIII on Hyper-Kvasir and LAG datasets. Starting from CCD [12], we notice that the use of MedMix can improve the AUC on both datasets by 1%. Replacing the CCD by the MSACL loss provides another improvement of between 1% and 2%. Then, adding the temperature calibration from (7) provides another improvement of about 0.5%.

2) *Different strong augmentations*: In Table IX, we explore the influence of strong augmentation strategies, represented by rotation, permutation, cutout, Gaussian noise and our proposed MedMix on the AUC results on Hyper-Kvasir and Covid-X datasets, based on our self-supervised MSACL pre-training with IGD as anomaly detector. The performance of our MedMix reaches the SOTA results of 99.5% and 87.2% on those datasets. The second best AUC (96.9%) on Hyper-Kvasir uses random permutations, which were used in our previously proposed CCD pre-training [12], producing an AUC 0.2% worse than our MedMix. For Covid-X, rotation is the second best data augmentation approach with an AUC result that is 5.1% worse than MedMix. Other approaches do not work well with the appearance characteristics of X-ray images, yielding significantly worse results than our MedMix on Covid-X. These results suggest that the use of MedMix as the strong augmentation yields the best AUC results on different medical image benchmarks.

3) *Different self-supervised methods*: In Table X, we show the results on Hyper-Kvasir from different pre-training approaches, using PaDiM as anomaly detector. It can be observed that our MSACL approach surpasses our previously proposed CCD pre-training [12] by 2.2% AUC. Other pre-training methods proposed in computer vision (e.g., ImageNet pre-training, SimCLR [29], Rot-Net [27]) achieve worse results than CCD and MSACL. An interesting point in this comparison is the poor result from ImageNet pre-training, suggesting that it may not generalise well for anomaly detection in medical images.

## IV. CONCLUSION

In this paper, we proposed a new self-supervised pre-training approach, namely MSACL, for UAD methods. MSACL is trained using the distribution of different strong augmentation distributions exploring contrastive learning and



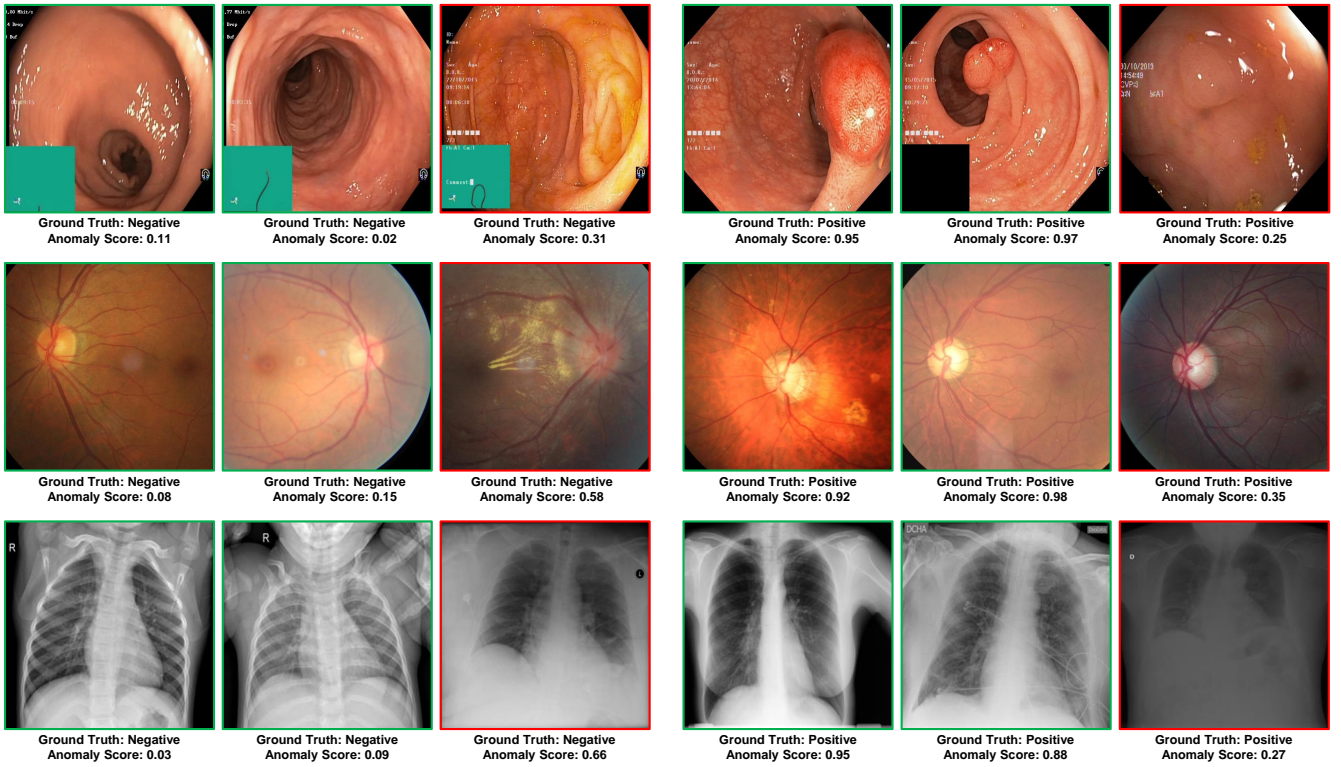


Fig. 6: Visual detection results and anomaly scores produced by the MSACL pre-trained IGD on three different datasets: Hyper-Kvasir (top), LAG (middle), Covid-X (bottom). Anomaly scores  $> 0.5$  classifies the image as positive, otherwise, the image is classified as negative. Correctly classified images are marked with green boxes, and incorrectly classified cases are marked with red boxes.

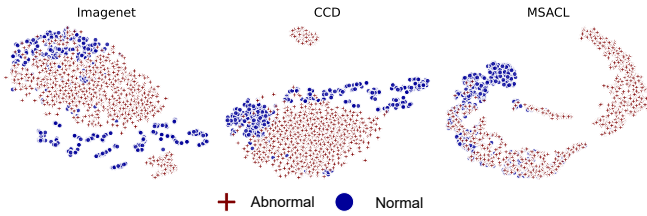


Fig. 7: t-SNE results of different pre-training approaches on the test set of Hyper-Kvasir. In contrast to ImageNet and CCD pre-trained models, MSACL clusters the normal image representations in a constrained region, and appears to separate the three strong augmentations into three distinct clusters.

clustering techniques. After pre-training using our MSACL, we fine-tune two SOTA predictive and generative anomaly detectors. The experimental results indicate that our MSACL pre-training can effectively improve the performance of anomaly detection and segmentation on several medical datasets for both anomaly detectors. In the future, we plan to design a new anomaly detector that suits better the characteristics of our self-supervised MSACL pre-training.

## REFERENCES

[1] Y. Tian *et al.*, “One-stage five-class polyp detection and classification,” in *2019 IEEE 16th International Symposium on Biomedical Imaging (ISBI 2019)*. IEEE, 2019, pp. 70–73.

Methods	AUC - Hyper	AUC - Covid-X
Rotate	0.969	0.821
Permutation	0.993	0.769
Cutout	0.905	0.709
Gaussian noise	0.939	0.732
MedMix	<b>0.995</b>	<b>0.872</b>

TABLE IX: Anomaly detection testing results in terms of different types of strong augmentations on Hyper-Kvasir and Covid-X. IGD [13] is used as the anomaly detector. Best results are highlighted.

Methods	AUC	Specificity	Sensitivity	Accuracy
ImageNet	0.923	0.816	0.909	0.883
SimCLR [29]	0.945	0.794	0.942	0.914
Rot-Net [27]	0.938	0.856	0.905	0.905
CCD [12]	0.978	0.923	0.961	0.967
MSACL	<b>0.996</b>	<b>0.966</b>	<b>0.981</b>	<b>0.983</b>

TABLE X: Ablation studies with different self-supervised pre-training approaches on Hyper-Kvasir testing set. PaDiM [35] is used as the anomaly detector. Best results are highlighted.

[2] Y. Tian, G. Maicas, L. Z. C. T. Pu, R. Singh, J. W. Verjans, and G. Carneiro, “Few-shot anomaly detection for polyp frames from colonoscopy,” in *International Conference on Medical Image Computing and Computer-Assisted Intervention*. Springer, 2020, pp. 274–284.

[3] Y. Liu, Y. Tian, G. Maicas, L. Z. Cheng Tao Pu, R. Singh, J. W. Verjans, and G. Carneiro, “Photoshopping colonoscopy video frames,” in *ISBI*, 2020, pp. 1–5.

[4] G. Litjens *et al.*, “A survey on deep learning in medical image analysis,” *Medical image analysis*, vol. 42, pp. 60–88, 2017.

[5] C. Baur, B. Wiestler, S. Albarqouni, and N. Navab, “Scale-space

- autoencoders for unsupervised anomaly segmentation in brain mri,” in *MICCAI*. Springer, 2020, pp. 552–561.
- [6] D.-P. Fan, G.-P. Ji, T. Zhou, G. Chen, H. Fu, J. Shen, and L. Shao, “Pranet: Parallel reverse attention network for polyp segmentation,” in *MICCAI*. Springer, 2020, pp. 263–273.
  - [7] C. T. P. LZ *et al.*, “Computer-aided diagnosis for characterisation of colorectal lesions: a comprehensive software including serrated lesions,” *Gastrointestinal Endoscopy*, 2020.
  - [8] F. Liu, Y. Tian *et al.*, “Self-supervised mean teacher for semi-supervised chest x-ray classification,” *arXiv preprint arXiv:2103.03629*, 2021.
  - [9] F. Liu, Y. Tian, F. R. Cordeiro, V. Belagiannis, I. Reid, and G. Carneiro, “Noisy label learning for large-scale medical image classification,” *arXiv preprint arXiv:2103.04053*, 2021.
  - [10] Y. Tian and others, “Detecting, localising and classifying polyps from colonoscopy videos using deep learning,” *arXiv preprint arXiv:2101.03285*, 2021.
  - [11] L. Pu, Z. C. Tao *et al.*, “Prospective study assessing a comprehensive computer-aided diagnosis for characterization of colorectal lesions: results from different centers and imaging technologies,” in *Journal of Gastroenterology and Hepatology*, vol. 34. WILEY 111 RIVER ST, HOBOKEN 07030-5774, NJ USA, 2019, pp. 25–26.
  - [12] Y. Tian, G. Pang, F. Liu, S. H. Shin, J. W. Verjans, R. Singh, G. Carneiro *et al.*, “Constrained contrastive distribution learning for unsupervised anomaly detection and localisation in medical images,” *MICCAI 2021*, 2021.
  - [13] Y. Chen, Y. Tian, G. Pang, and G. Carneiro, “Unsupervised anomaly detection and localisation with multi-scale interpolated gaussian descriptors,” *arXiv preprint arXiv:2101.10043*, 2021.
  - [14] X. Chen, S. You, K. C. Tezcan, and E. Konukoglu, “Unsupervised lesion detection via image restoration with a normative prior,” *Medical image analysis*, vol. 64, p. 101713, 2020.
  - [15] T. Schlegl *et al.*, “f-anogan: Fast unsupervised anomaly detection with generative adversarial networks,” *Medical image analysis*, vol. 54, pp. 30–44, 2019.
  - [16] P. Seeböck, J. I. Orlando, T. Schlegl, S. M. Waldstein, H. Bogunović, S. Klimesch, G. Langs, and U. Schmidt-Erfurth, “Exploiting epistemic uncertainty of anatomy segmentation for anomaly detection in retinal oct,” *IEEE transactions on medical imaging*, vol. 39, no. 1, pp. 87–98, 2019.
  - [17] D. Gong *et al.*, “Memorizing normality to detect anomaly: Memory-augmented deep autoencoder for unsupervised anomaly detection,” in *ICCV*, 2019, pp. 1705–1714.
  - [18] Y. Liu, Y. Tian, G. Maicas, L. Z. Cheng Tao Pu, R. Singh, J. W. Verjans, and G. Carneiro, “Photoshopping colonoscopy video frames,” in *ISBI*, 2020, pp. 1–5.
  - [19] S. Venkataramanan, K.-C. Peng, R. V. Singh, and A. Mahalanobis, “Attention guided anomaly localization in images,” in *ECCV*. Springer, 2020, pp. 485–503.
  - [20] Y. Tian *et al.*, “Weakly-supervised video anomaly detection with robust temporal feature magnitude learning,” *arXiv preprint arXiv:2101.10030*, 2021.
  - [21] G. Pang, C. Shen, and A. van den Hengel, “Deep anomaly detection with deviation networks,” in *Proceedings of the 25th ACM SIGKDD International Conference on Knowledge Discovery & Data Mining*, 2019, pp. 353–362.
  - [22] L. Ruff, R. Vandermeulen, N. Goernitz, L. Deecke, S. A. Siddiqui, A. Binder, E. Müller, and M. Kloft, “Deep one-class classification,” in *International conference on machine learning*. PMLR, 2018, pp. 4393–4402.
  - [23] Y. Chen, X. S. Zhou, and T. S. Huang, “One-class svm for learning in image retrieval,” in *Proceedings 2001 International Conference on Image Processing (Cat. No. 01CH37205)*, vol. 1. IEEE, 2001, pp. 34–37.
  - [24] S. Akcay, A. Atapour-Abarghouei, and T. P. Breckon, “Ganomaly: Semi-supervised anomaly detection via adversarial training,” in *Asian conference on computer vision*. Springer, 2018, pp. 622–637.
  - [25] G. Pang, C. Shen, L. Cao, and A. V. D. Hengel, “Deep learning for anomaly detection: A review,” *ACM Computing Surveys (CSUR)*, vol. 54, no. 2, pp. 1–38, 2021.
  - [26] D. Hendrycks *et al.*, “Using self-supervised learning can improve model robustness and uncertainty,” *arXiv preprint arXiv:1906.12340*, 2019.
  - [27] I. Golan and R. El-Yaniv, “Deep anomaly detection using geometric transformations,” *arXiv preprint arXiv:1805.10917*, 2018.
  - [28] L. Bergman and Y. Hoshen, “Classification-based anomaly detection for general data,” *arXiv preprint arXiv:2005.02359*, 2020.
  - [29] T. Chen, S. Kornblith, M. Norouzi, and G. Hinton, “A simple framework for contrastive learning of visual representations,” in *ICML*. PMLR, 2020, pp. 1597–1607.
  - [30] K. He *et al.*, “Momentum contrast for unsupervised visual representation learning,” in *CVPR*, 2020, pp. 9729–9738.
  - [31] F. Liu *et al.*, “Self-supervised depth estimation to regularise semantic segmentation in knee arthroscopy,” in *International Conference on Medical Image Computing and Computer-Assisted Intervention*. Springer, 2020, pp. 594–603.
  - [32] J. Tack, S. Mo, J. Jeong, and J. Shin, “Csi: Novelty detection via contrastive learning on distributionally shifted instances,” *arXiv preprint arXiv:2007.08176*, 2020.
  - [33] T. Wang and P. Isola, “Understanding contrastive representation learning through alignment and uniformity on the hypersphere,” in *ICML*. PMLR, 2020, pp. 9929–9939.
  - [34] M.-S. To, I. G. Sarno, C. Chong, M. Jenkinson, and G. Carneiro, “Self-supervised lesion change detection and localisation in longitudinal multiple sclerosis brain imaging,” *arXiv preprint arXiv:2106.00919*, 2021.
  - [35] T. Defard, A. Setkov, A. Loesch, and R. Audigier, “Padim: a patch distribution modeling framework for anomaly detection and localization,” *arXiv preprint arXiv:2011.08785*, 2020.
  - [36] H. Borgli and *et al.*, “Hyperkvasir, a comprehensive multi-class image and video dataset for gastrointestinal endoscopy,” *Scientific Data*, vol. 7, no. 1, pp. 1–14, 2020.
  - [37] L. Li *et al.*, “Attention based glaucoma detection: A large-scale database and cnn model,” in *CVPR*, 2019, pp. 10571–10580.
  - [38] L. Wang, Z. Q. Lin, and A. Wong, “Covid-net: A tailored deep convolutional neural network design for detection of covid-19 cases from chest x-ray images,” *Scientific Reports*, vol. 10, no. 1, pp. 1–12, 2020.
  - [39] T. Reiss and Y. Hoshen, “Mean-shifted contrastive loss for anomaly detection,” *arXiv preprint arXiv:2106.03844*, 2021.
  - [40] C. Doersch, A. Gupta, and A. A. Efros, “Unsupervised visual representation learning by context prediction,” in *ICCV*, 2015, pp. 1422–1430.
  - [41] S. Yun, D. Han, S. J. Oh, S. Chun, J. Choe, and Y. Yoo, “Cutmix: Regularization strategy to train strong classifiers with localizable features,” in *Proceedings of the IEEE/CVF International Conference on Computer Vision*, 2019, pp. 6023–6032.
  - [42] Z. Wang and *et al.*, “Multiscale structural similarity for image quality assessment,” in *The Thirty-Seventh Asilomar Conference on Signals, Systems & Computers*, 2003, vol. 2. Ieee, 2003, pp. 1398–1402.
  - [43] D. Berthelot, C. Raffel, A. Roy, and I. Goodfellow, “Understanding and improving interpolation in autoencoders via an adversarial regularizer,” *arXiv preprint arXiv:1807.07543*, 2018.
  - [44] K. He *et al.*, “Deep residual learning for image recognition,” in *CVPR*, 2016, pp. 770–778.
  - [45] K. Sohn, C.-L. Li, J. Yoon, M. Jin, and T. Pfister, “Learning and evaluating representations for deep one-class classification,” *arXiv preprint arXiv:2011.02578*, 2020.
  - [46] P. Bergmann, M. Fauser, D. Sattlegger, and C. Steger, “Uninformed students: Student-teacher anomaly detection with discriminative latent embeddings,” in *Proceedings of the IEEE/CVF Conference on Computer Vision and Pattern Recognition*, 2020, pp. 4183–4192.
  - [47] J. Masci and *et al.*, “Stacked convolutional auto-encoders for hierarchical feature extraction,” in *International Conference on Artificial Neural Networks*. Springer, 2011, pp. 52–59.
  - [48] P. Perera, R. Nallapati, and B. Xiang, “Ogan: One-class novelty detection using gans with constrained latent representations,” in *CVPR*, 2019, pp. 2898–2906.
  - [49] O. Ronneberger, P. Fischer, and T. Brox, “U-net: Convolutional networks for biomedical image segmentation,” in *International Conference on Medical image computing and computer-assisted intervention*. Springer, 2015, pp. 234–241.
  - [50] Z. Zhou *et al.*, “Unet++: A nested u-net architecture for medical image segmentation,” in *Deep learning in medical image analysis and multimodal learning for clinical decision support*. Springer, 2018, pp. 3–11.
  - [51] F. I. Diakogiannis *et al.*, “Resunet-a: a deep learning framework for semantic segmentation of remotely sensed data,” *ISPRS Journal of Photogrammetry and Remote Sensing*, vol. 162, pp. 94–114, 2020.
  - [52] Y. Fang, C. Chen, Y. Yuan, and K.-y. Tong, “Selective feature aggregation network with area-boundary constraints for polyp segmentation,” in *MICCAI*. Springer, 2019, pp. 302–310.